# Decoupling the Metal—Insulator Transition Temperature and Hysteresis of VO2 Using Ge Alloying and Oxygen Vacancies

## COMMUNICATION

# Decoupling the Metal—Insulator Transition Temperature and Hysteresis of VO₂ Using Ge Alloying and Oxygen Vacancies

Parker Schofield,[a,b,¶] Erick J. Braham,[a,b,¶] Baiyu Zhang,[b,¶] Justin L. Andrews,[a,b] Hayley Drozdick,[a] Dexin Zhao,[b] Wasif Zaheer,[a,b] Rebeca Gurrola,[b] Kelvin Xie,[b] Patrick J. Shamberger,[b] Xiaofeng Qian,[b,c*] Sarbajit Banerjee[a,b*]

**The metal-to-insulator transition of VO₂ underpins applications in thermochromics, neuromorphic computing, and infrared vision. Ge alloying is shown to elevate the transition temperature by promoting V—V dimerization, thereby expanding the stability of the monoclinic phase to higher temperatures. By suppressing the propensity for oxygen vacancy formation, Ge alloying renders the hysteresis of the transition exquisitely sensitive to oxygen stoichiometry.**

VO₂ is a canonical example of a strongly electron-correlated material with close coupling of spin, charge, orbital, lattice, and atomic degrees of freedom.[1–3] It exhibits a pronounced near-room-temperature metal-to-insulator transition (MIT) at approx. 67°C, which is accompanied by the displacive rearrangement of atoms from a low-temperature (and lower-symmetry) monoclinic (M1) phase to a high-temperature and higher-symmetry rutile (R) phase.[4–8] The ultrafast transition results in a profound modulation of physical properties such as electrical conductivity, infrared transmittance, and thermal conductivity.[1,5,6,9] A particular challenge for strongly correlated materials is to systematically tune and disentangle different transformation characteristics. Substitutional incorporation of alloyant atoms has been used to tune the relative thermodynamic stabilities of the monoclinic and rutile phases, but with a few exceptions engenders suppression of the critical transition temperature.[10–14] Dopant atoms can profoundly modify local atomistic and electronic structure. In this communication, we decipher the mechanistic origins of the unusual elevation of transition temperature observed upon alloying of VO₂ with Ge and demonstrate the decoupling of transition temperature and hysteresis of the MIT through control of Ge alloying and its effects on oxygen stoichiometry.

Germanium alloying in particular has been observed to raise the transition temperature to approx. 95°C (up from approx. 67°C in undoped VO₂) for VO₂ thin films.[15] As a prime material candidate demonstrating neuronal functionality needed for next-generation neuromorphic computing applications,[9] VO₂ stands to benefit greatly by incorporating Ge to modulate MIT activity to fall within 80—100°C operating environments of scaled circuit elements in neuromorphic hardware.[1,9] Greater understanding of the mechanisms by which Ge modulates the MIT is paramount to achieve the desired operating temperatures. In order to investigate the underpinnings of increased stabilization of the M1-phase relative to R-phase upon Ge incorporation, Ge-alloyed VO₂ particles have been synthesized via two distinct methods: hydrothermal synthesis and solid-state synthesis. This allows for comparison of alloyant germanium influences in oxygen-rich and oxygen-poor environments.

**Figure 1A-B** exhibits TEM images of nanobeams characteristic of the morphology of hydrothermally prepared Ge₀.₀₂V₀.₉₈O₂. **Figure 1C-D** shows SEM images of "meatball" structures of Ge₀.₀₄V₀.₉₆O₂ particles prepared by solid-state synthesis. Powder X-ray diffraction patterns at room temperature are indexed to M1-phase VO₂ (**Figure 1F**). A Rietveld refinement performed on XRD patterns (**Figure 1E, Table S1**) shows stabilization of phase-pure monoclinic VO₂ (space group $P2_1/c$). EDX maps in **Figure 1G-H** (and **Fig. S1**) corroborate homogeneous Ge incorporation in both samples. **Figure 1I** and **Figure S2** exhibit X-ray diffraction patterns acquired in 5°C increments for heating and cooling of hydrothermally prepared Ge-alloyed VO₂. At approx. 85—90°C, during the initial heating process, the monoclinic (011) reflection is supplanted by a rutile (110) reflection, reflecting the first-order transition of the material from a M1-phase to R-phase (substantially elevated above the 67°C transition of unalloyed VO₂).[13] A pronounced hysteresis is observed upon cooling in the 70—40°C range.

**Figure 2A** contrasts differential scanning calorimetry (DSC) traces of Ge-alloyed VO₂ prepared by the two synthetic methods. The red trace for solid-state-synthesized Ge₀.₀₄V₀.₉₆O₂ displays an elevated transition temperature as well as a

---

[a.] Department of Chemistry, Texas A&M University, College Station, TX 77843, USA
[b.] Department of Materials Science and Engineering, Texas A&M University, College Station, TX 77843, USA
[c.] Department of Electrical and Computer Engineering, Texas A&M University, College Station, TX 77843, USA
¶These authors contributed equally to this work.
E-mail: feng@tamu.edu banerjee@chem.tamu.edu
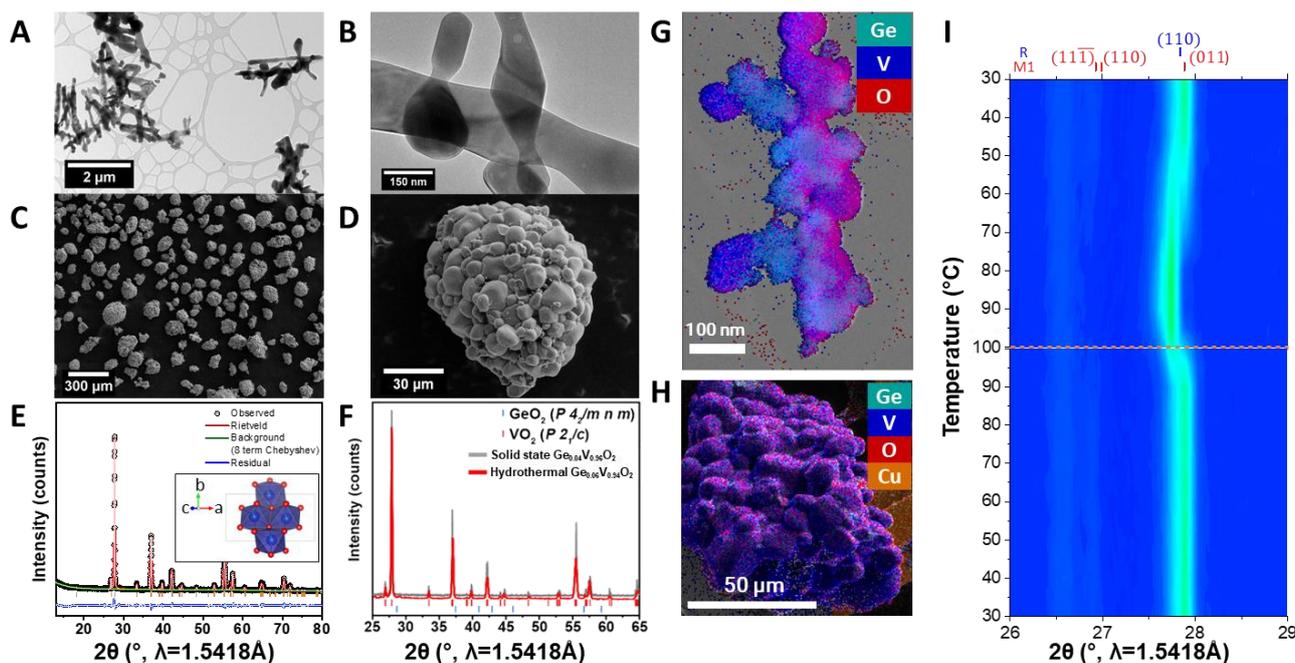
**Figure 1** A,B) TEM images of hydrothermally prepared $Ge_{0.02}V_{0.98}O_2$ nanobeams (144 ± 80 nm). C,D) SEM images of solid-state-prepared $Ge_{0.04}V_{0.96}O_2$ particles (8.0 3.3 µm) sintered into an agglomerate. E) Rietveld refinement of hydrothermally prepared $Ge_{0.06}V_{0.94}O_2$ (the structure of monoclinic $VO_2$ crystallized in the $P2_1/c$ group is shown in the inset). F) Powder X-ray diffraction patterns of hydrothermally prepared and solid-state-prepared $Ge_xV_{1-x}O_2$. EDX mapping of Ge (cyan), V (blue), and O (red) across G) hydrothermally prepared $Ge_{0.02}V_{0.98}O_2$ nanowires. H) a solid-state-prepared $Ge_{0.04}V_{0.96}O_2$ "meatball" structure. I) temperature-dependent powder X-ray diffraction of hydrothermally prepared $Ge_{0.06}V_{0.94}O_2$ heated and cooled across its monoclinic—rutile structural transition.

hysteresis similar to that of unalloyed $VO_2$.[13] The hydrothermally prepared sample (blue) displays asymmetric heating and cooling transitions with an extremely broad, non-Gaussian, cooling transition with multiple exothermic features. **Figures 2B-C** show DSC traces for increasing concentrations of Ge precursor added in hydrothermally prepared and solid-state-prepared $Ge_xV_{1-x}O_2$, respectively. Both synthetic methods feature increasing MIT equilibrium transition temperature ($T_{eq}$) upon increasing Ge content. Rate-variant DSC traces in **Figure S3** do not show an appreciable rate-dependence of transition temperatures suggesting that the density of nucleation sites is not appreciably modified by changing the rates in this range of scan rates.[13] **Figures 2D-E** show the cooling and heating transitions measured for 299 individual hydrothermally prepared particles by optical microscopy.[16] These results illustrate that the heating and cooling transitions have different dependences on the extent of alloying— greater Ge alloying is correlated with increased suppression of the cooling transition— and that the binned sizes of particles do not strongly adhere to hysteresis isopleths, which indicates that hysteresis is not well correlated with particle size.

Asymmetry between heating and cooling transitions has been reported previously in doped $VO_2$, and is attributable to the distinctive modes of nucleation of the M1→R and R→M1 transitions.[13,17] Whereas the former is nucleated at twin planes in the M1 phase, the latter is mediated by point defects such as oxygen vacancies.[13,17,18] Given the comparable Ge content between the solid-state- and hydrothermally-prepared samples ($Ge_{0.04}V_{0.96}O_2$ and $Ge_{0.06}V_{0.94}O_2$, respectively), the origin of their drastic differences in hysteresis and cooling transition temperature must relate to their synthesis methodologies and

their corresponding effects on composition and structure. A primary difference between hydrothermal and solid-state methods is the oxygen chemical potential. Hydrothermal synthesis involves the 2-propanol reduction of aqueous $HVO_3$ precursor in the presence of $GeO_2$ under temperatures and redox potentials that favour formation of $VO_2$ as per the Pourbaix diagram. In contrast, solid-state synthesis involves mixing and sintering of $VO_2$ and $GeO_2$ powders at 900°C in a sealed fused silica ampoule. The former corresponds to oxygen-rich, whereas the latter corresponds to oxygen-poor conditions.
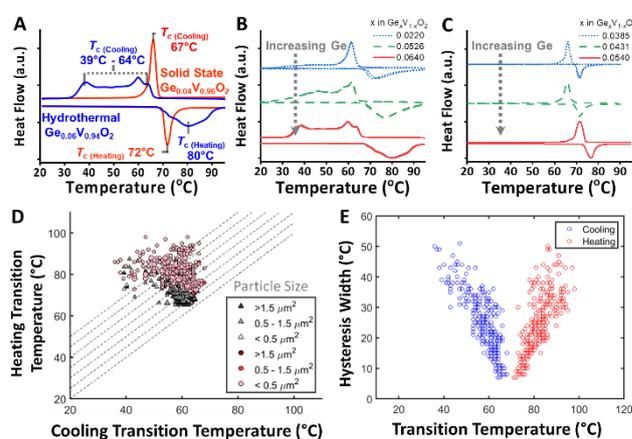


**Figure 2**. A) Differential scanning calorimetry of hydrothermally prepared and solid-state-prepared $Ge_xV_{1-x}O_2$. B) Differential scanning calorimetry of hydrothermally prepared $Ge_xV_{1-x}O_2$ with increasing Ge content. C) Differential scanning calorimetry of solid-state-prepared $Ge_xV_{1-x}O_2$ with increasing Ge content. D) Transition temperature distribution of hydrothermally prepared $Ge_{0.06}V_{0.94}O_2$ as a function of particle size. E) Transition temperature distribution of $Ge_{0.06}V_{0.94}O_2$ highlighting the differing dependencies on Ge concentration for heating and cooling transitions.

**COMMUNICATION**

Indeed, neutron activation analysis has been performed in triplicate on three distinct samples, the average V:O ratio is measured as 0.492±0.017 for hydrothermal samples and 0.541±0.021 for the solid-state products (**Figure S4**), reflecting the relative oxygen scarcity for the latter preparatory method. Density functional theory (DFT) calculations[19] have further been performed to assess formation energies of $Ge_xV_{1-x}O_2$ with the alloyant Ge placed in different sites under different oxygen potentials (**Figure 3A**-**B**). Ge is strongly favored to be a substitutional alloyant on the cation sublattice ($Ge_V$) as compared to being a alloyant on the anion lattice ($Ge_O$) or an interstitial alloyant ($Ge_i$). Hard X-ray photoelectron spectroscopy (HAXPES) contrasting unalloyed $VO_2$ and hydrothermally prepared $Ge_{0.06}V_{0.94}O_2$ in **Figure 4A** indeed corroborates the incorporation of formally tetravalent germanium in $Ge_xV_{1-x}O_2$, which is corroborated by Ge L-edge X-ray absorption near edge structure (XANES) measurements in Figure S5

Further calculations queried the role of oxygen chemical potential. **Figures 3C**-**D** shows energies of several charged defects in oxygen-poor and oxygen-rich settings, including Ge substitutionally incorporated at a vanadium site ($Ge_V$), oxygen vacancy in unalloyed $VO_2$ ($vac_O$), and an oxygen vacancy in the presence of a germanium alloyant ($Ge_V + vac_O$). Notably, the formation energy of an oxygen vacancy is higher than the formation energy of a germanium alloyant defect. Intuitively, oxygen vacancies have lower defect formation energy in O-poor conditions than O-rich conditions. For both oxygen-poor and oxygen-rich scenarios, the presence of doped germanium increases the energetic cost of oxygen vacancy formation as compared to unalloyed cases, since the defect complex ($Ge_V + vac_O$) has a formation energy than Ge substitutional defects ($Ge_V$). In other words, Ge alloying inhibits oxygen vacancy formation regardless of the oxygen chemical potential. Contrasting Figures 3C and D, (i) oxygen vacancy formation is more strongly suppressed under oxygen-rich conditions and (ii) formation energies for oxygen vacancy formation are consistently lower under O-poor conditions. Of possible point defect types, oxygen vacancies are known to be potent nucleation sites for phase transitions in $VO_2$.[13,16,17] As such, the incorporation of $Ge_V$—strongly suppressing $vac_O$ formation— has substantial implications for nucleation of the cooling transition in $VO_2$. Since the relatively oxygen-abundant hydrothermal synthesis yields a relatively lower density of oxygen vacancies, these samples required increased overcooling to nucleate the monoclinic phase during cooling (**Figure 2**). Notably, it is the particular role of Ge in suppressing oxygen vacancy formation that gives rise to an asymmetric transition and enables sensitive modulation of the hysteresis.

The origins of the elevated transition temperature have been examined using DFT calculations.[20] The relaxed geometries of monoclinic phases of unalloyed and Ge-alloyed $VO_2$ are shown in **Figures 3E**-**F**. In M1 unalloyed $VO_2$, characteristic V—V dimers are observed with a consistent separation of 2.877Å with the dimers themselves being spaced 3.109Å apart along the *a*-axis. Upon Ge alloying, the V—V dimers are more strongly paired with a separation of 2.856Å with dimers themselves spaced
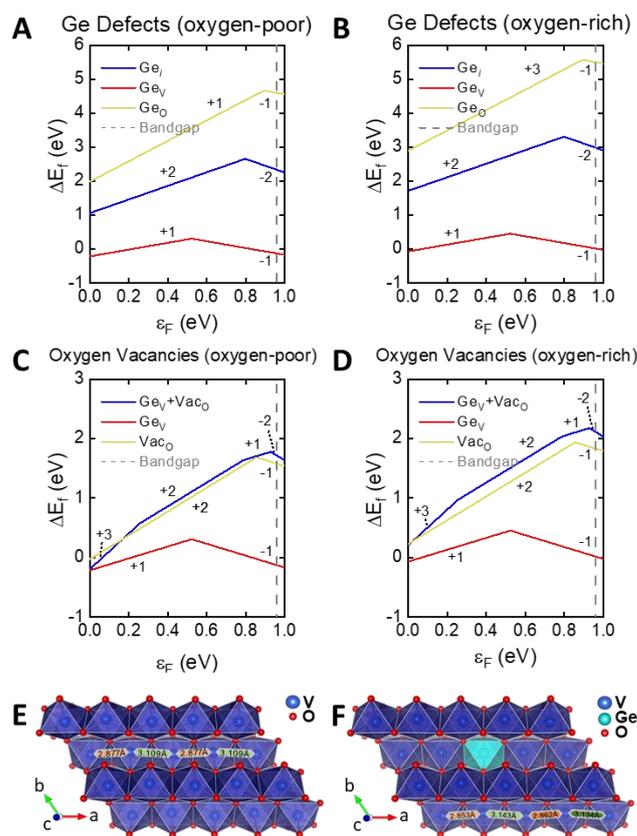


Figure 3. A,B) DFT-calculated formation energies of Ge interstitials, $Ge_V$, and $Ge_O$ formed in O-poor and O-rich settings, marked with the most stable charge states of the defect. C,D) DFT-calculated formation energies of O vacancies, $Ge_V$ substitutional alloying, and combined O vacancies with $Ge_V$ substitution in O-poor and O-rich settings. E) DFT-relaxed structure of $VO_2$ featuring V—V dimers with bond distances regularly alternating between 2.877Å and 3.109Å. F) DFT-relaxed structure of Ge-alloyed $VO_2$ demonstrating the enhanced pairing of V—V dimers (bond distances alternating between 2.853Å and 3.143Å).

3.140Å from each other (**Table S2**). The symmetry-raising M1→R structural phase transformation in $VO_2$ requires depairing of the V—V dimers, formally a Peierls-type transition.[1,3,8] As such, by forming stronger V—V dimers (2.856Å separation down from 2.877Å), Ge alloying stabilizes the M1 phase up to higher temperatures. While the monoclinic phase is stabilized up to a higher temperature as compared to the rutile phase, the extent of supercooling is governed by the oxygen stoichiometry, which depends on both alloying and the synthesis conditions, thereby providing a means to disentangle the MIT transition temperature and hysteresis.

XANES spectra were collected at V $L_{2,3}$- and O K-edges of unalloyed $VO_2$ and $Ge_xV_{1-x}O_2$ (**Fig. 4**, **Fig. S5**).[21,22] The V $L_2$ and $L_3$ transitions (corresponding to V 2p—V 3d excitations) of unalloyed and Ge-alloyed $VO_2$ are closely overlapped. The O K-edge has two separate manifolds as a result of approximately octahedral crystal field splitting of V 3d orbitals with $t_{2g}$ and $e_g$ symmetry.[23] In comparing Ge-alloyed and unalloyed samples, the O K-edge absorption features are reduced in intensity with respect to the V L-edge features, suggesting reduced overall O3p—V3d hybridization in $Ge_xV_{1-x}O_2$ as a result of subtle structural transformations caused by Ge increasing V—V dimerization.

Extended X-ray absorption fine structure (EXAFS) spectra were
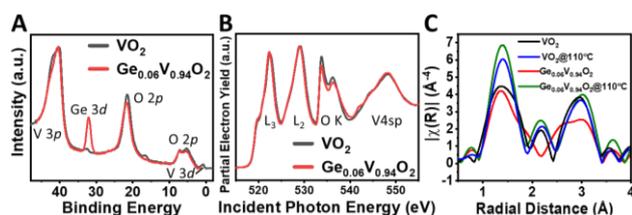
**Figure 4.** A) HAXPES contrasting undoped VO$_2$ and hydrothermally prepared Ge$_{0.06}$V$_{0.94}$O$_2$. B) XANES collected on VO$_2$ and hydrothermally prepared Ge$_{0.06}$V$_{0.94}$O$_2$. C) EXAFS radial distance plot for data collected at room temperature and at 110 °C for both unalloyed VO$_2$ and Ge$_{0.06}$V$_{0.94}$O$_2$.

collected for VO$_2$ and Ge$_x$V$_{1-x}$O$_2$ ($x \sim 0.06$) at room temperature and at 110°C, to fit structural information on both M1 and R states, respectively (**Figure 4C, Figure S6, Table S3**). Upon Ge-alloying, first shell analysis suggests that the long V—O bonds are elongated further and short bonds are further shortened in the M1 phase, supporting exaggerated dimerization. In the R state, Ge-alloying shortens all bonds. In tandem with the XANES analysis, Ge incorporation alters the VO$_2$ structure by enhancing V—V dimerization, which alters the electronic structure of M$_1$ VO$_2$ through decreased orbital overlapping and hybridization. These results demonstrate synergistic local structure modifications to extend the range of M1 phase stability in the phase diagram of Ge$_x$V$_{1-x}$O$_2$. DFT calculations reveal that substitutional Ge incorporation inhibits oxygen vacancy formation and promotes increased V—V dimerization. Nucleation plays a governing role in the cooling transition of the metal-to-insulator transition, and differences in potent nucleation sites in the form of oxygen vacancies underlies differences in the cooling transition of Ge$_x$V$_{1-x}$O$_2$ prepared by two separate synthetic methods (in contrast, the heating transition is governed by domain walls). In particular, hydrothermally prepared Ge$_x$V$_{1-x}$O$_2$ features a broad, non-Gaussian cooling transition arising from the greater inhibition of oxygen vacancy formation during its synthesis as compared to solid-state-prepared Ge$_x$V$_{1-x}$O$_2$, which gives rise to nucleation limitations. The results thus demonstrate independent control of transformation temperature and hysteresis.

## Conflicts of interest

The authors declare no competing financial interest.

## References

1    J. L. Andrews, D. A. Santos, M. Meyyappan, R. S. Williams and S. Banerjee, *Trends Chem.*, 2019, **1**, 711–726.

2    J. D. Budai, J. Hong, M. E. Manley, E. D. Specht, C. W. Li, J. Z. Tischler, D. L. Abernathy, A. H. Said, B. M. Leu, L. A. Boatner, R. J. McQueeney and O. Delaire, *Nature*, 2014, **515**, 535–539.

3    W. H. Brito, M. C. O. Aguiar, K. Haule and G. Kotliar, *Phys. Rev. Lett.*, 2016, **117**, 1–6.

4    J. Jeong, N. Aetukuri, T. Graf, T. D. Schladt, M. G. Samant and S. S. P. Parkin, *Science (80-. ).*, 2013, **339**, 1402–1406.

5    X. Cao, T. Chang, Z. Shao, F. Xu, H. Luo and P. Jin, *Matter*, 2020, **2**, 862–881.

6    Y. Cui, Y. Ke, C. Liu, Z. Chen, N. Wang, L. Zhang, Y. Zhou, S. Wang, Y. Gao and Y. Long, *Joule*, 2018, **2**, 1707–1746.

7    D. G. Sellers, E. J. Braham, R. Villarreal, B. Zhang, A. Parija, T. D. Brown, T. E. G. Alivio, H. Clarke, L. R. De Jesus, L. Zuin, D. Prendergast, X. Qian, R. Arroyave, P. J. Shamberger and S. Banerjee, *J. Am. Chem. Soc.*, 2020, **142**, 15513–15526.

8    S. Wall, S. Yang, L. Vidas, M. Chollet, J. M. Glownia, M. Kozina, T. Katayama, T. Henighan, M. Jiang, T. A. Miller, D. A. Reis, L. A. Boatner, O. Delaire and M. Trigo, *Science (80-. ).*, 2018, **362**, 572–576.

9    W. Yi, K. K. Tsang, S. K. Lam, X. Bai, J. A. Crowell and E. A. Flores, *Nat. Commun.*, 2018, **9**, 1–10.

10    H. Asayesh-Ardakani, A. Nie, P. M. Marley, Y. Zhu, P. J. Phillips, S. Singh, F. Mashayek, G. Sambandamurthy, K. Bin Low, R. F. Klie, S. Banerjee, G. M. Odegard and R. Shahbazian-Yassar, *Nano Lett.*, 2015, **15**, 7179–7188.

11    A. Krammer, A. Magrez, W. A. Vitale, P. Mocny, P. Jeanneret, E. Guibert, H. J. Whitlow, A. M. Ionescu and A. Schüler, *J. Appl. Phys.*, 2017, **122**, 45304.

12    Y. Wu, L. Fan, Q. Liu, S. Chen, W. Huang, F. Chen, G. Liao, C. Zou and Z. Wu, *Sci. Rep.*, 2015, **5**, 1–8.

13    E. J. Braham, D. Sellers, E. Emmons, R. Villarreal, H. Asayesh-Ardakani, N. A. Fleer, K. E. Farley, R. Shahbazian-Yassar, R. Arròyave, P. J. Shamberger and S. Banerjee, *Chem. Mater.*, 2018, **30**, 214–224.

14    C. E. Wilson, A. E. Gibson, J. J. Argo, P. A. Loughney, W. Xu, G. King and V. Doan-Nguyen, *J. Mater. Res.*, 2021, **36**, 268–280.

15    A. Krammer, A. Magrez, W. A. Vitale, P. Mocny, P. Jeanneret, E. Guibert, H. J. Whitlow, A. M. Ionescu and A. Schüler, *J. Appl. Phys.*, 2017, **122**, 45304.

16    H. Clarke, B. D. Caraway, D. G. Sellers, E. J. Braham, S. Banerjee, R. Arróyave and P. J. Shamberger, *Phys. Rev. Mater.*, 2018, **2**, 1–8.

17    W. Fan, J. Cao, J. Seidel, Y. Gu, J. W. Yim, C. Barrett, K. M. Yu, J. Ji, R. Ramesh, L. Q. Chen and J. Wu, *Phys. Rev. B - Condens. Matter Mater. Phys.*, 2011, **83**, 235102.

18    A. Yano, H. Clarke, D. G. Sellers, E. J. Braham, T. E. G. Alivio, S. Banerjee and P. J. Shamberger, *J. Phys. Chem. C*, 2020, **124**, 21223–21231.

19    G. Kresse and J. Furthmüller, *Comput. Mater. Sci.*, 1996, **6**, 15–50.

20    A. V. Krukau, O. A. Vydrov, A. F. Izmaylov and G. E. Scuseria, *J. Chem. Phys.*, 2006, **125**, 224106-1-224106–5.

21    M. G. Brik, K. Ogasawara, H. Ikeno and I. Tanaka, *Eur. Phys. J. B*, 2006, **51**, 345–355.

22    F. Frati, M. O. J. Y. Hunault and F. M. F. De Groot, *Chem. Rev.*, 2020, **120**, 4056–4110.

23    M. Abbate, H. Pen, M. T. Czyzyk, F. M. F. de Groot, J. C. Fuggle, Y. J. Ma, C. T. Chen, F. Sette, A. Fujimori, Y. Ueda and K. Kosuge, *J. Electron Spectros. Relat. Phenomena*, 1993, **62**, 185–195.